Tunable single quantum dot nanocavities for cavity QED experiments

2008 J. Phys.: Condens. Matter 20 454209

(http://iopscience.iop.org/0953-8984/20/45/454209)

J. Phys.: Condens. Matter **20** (2008) 454209 (8pp) doi:10.1088/0953-8984/20/45/454209

Tunable single quantum dot nanocavities for cavity QED experiments

M Kaniber, A Laucht, A Neumann, M Bichler, M-C Amann and J J Finley

Walter Schottky Institut and Technische Universität München, Am Coulombwall 3, D-85748 Garching bei München, Germany

E-mail: michael.kaniber@wsi.tum.de

Received 13 June 2008
Published 23 October 2008
Online at stacks.iop.org/JPhysCM/20/454209

Abstract

We present cavity quantum electrodynamics experiments performed on single quantum dots embedded in two-dimensional photonic crystal nanocavities. We begin by describing the structural and optical properties of the quantum dot sample and the photonic crystal nanocavities and compare the experimental results with three-dimensional calculations of the photonic properties. The influence of the tailored photonic environment on the quantum dot spontaneous emission dynamics is studied using spectrally and spatially dependent time-resolved spectroscopy. In ensemble and single dot measurements we show that the photonic crystals strongly enhance the photon extraction efficiency and, therefore, are a promising concept for realizing efficient single-photon sources. Furthermore, we demonstrate single-photon emission from an individual quantum dot that is spectrally detuned from the cavity mode. The need for controlling the spectral dot–cavity detuning is discussed on the basis of shifting either the quantum dot emission via temperature tuning or the cavity mode emission via a thin film deposition technique. Finally, we discuss the recently discovered non-resonant coupling mechanism between quantum dot emission and cavity mode for large detunings which drastically lowers the purity of single-photon emission from dots that are spectrally coupled to nanocavity modes.

(Some figures in this article are in colour only in the electronic version)

1. Introduction

The coupling of single self-assembled quantum dots (QDs) to high quality, low mode volume optical nanocavities is highly desirable for fundamental experiments in solid-state quantum information science. One of the crucial components for both quantum cryptography [1], all optical quantum computation [2] and the realization of quantum repeaters [3] is a deterministic and efficient single-photon turnstile device, which emits on demand one and only one indistinguishable photon per excitation cycle. Indeed QDs give rise to single photons [4, 5] due to their zero-dimensional electronic density of states and the strongly anharmonic nature of their few-particle optical excitation spectrum. Therefore, QDs are often considered to be the solid-state analogues of atoms and are, thus, commonly termed to be *artificial atoms* in the solid state. Although QDs would be, in principle, perfect single-photon emitters they typically exhibit a very poor single-photon extraction efficiency $\eta \sim 1\%$ [6] due to the refractive index difference at the semiconductor–air interface. One possible solution for the efficiency problem is the incorporation of QDs into a photonic bandgap (PBG) material, which leads to spatial redistribution of the QD emission [7–9] and, therefore, gives rise to highly efficient single-photon generation [10]. An additional incorporation of defect nanocavities into the photonic crystal (PC) environment strongly influences the spontaneous emission (SE) dynamics of the embedded QDs [11] due to the Purcell effect [12]. Such enhancement of the QD SE rate provides the opportunity to realize single-photon sources with a very high degree of quantum indistinguishability [13, 14], a necessary criterion for the application of such devices in quantum computation and more sophisticated quantum optics experiments.

In this paper, we review our cavity quantum electrodynamics (cQED) experiments using self-assembled $In_{0.5}Ga_{0.5}As$ QDs embedded within PC nanostructures. We start with

describing the structural and optical properties of QDs and PC nanocavities and compare the latter with calculations of the photonic band structure of our devices. Applying continuous wave (cw) and time-resolved micro-photoluminescence (μ-PL) spectroscopy enables us to directly probe the influence of the modified photonic environment on the SE properties of the embedded QD ensemble. We observe a strong enhancement of the SE rate for QDs both spatially and spectrally in resonance with the defect nanocavity mode of 10×, when compared to QDs next to the PC nanostructure in the unpatterned region of the device. In strong contrast, we observe a 10× suppression of the SE rate for QDs emitting deep into the PBG. These measurements already indicate a strong enhancement of the photon extraction efficiency η for QDs embedded in PC nanostructures, which is then supported by single dot measurements performed on the same sample. For those dots, we present investigations of the photon statistics that show pronounced antibunching, a distinct signature of emission from a single quantum emitter. To observe strong cQED effects for single QDs, one requires both good spatial and spectral coupling of the dot emission to the PC nanocavity mode. Whilst the former is technologically quite challenging, the latter can either be achieved by tuning the *QD emission*, for instance by temperature tuning [15] or electric fields [16], or by tuning the *cavity mode*, for instance by digital etching [17] or inert gas deposition techniques [18]. Some of these approaches are described before we finally discuss a recently discovered mechanism which indicates the presence of a hitherto unidentified coupling between a single QD and a cavity mode even for spectral detunings up to 19 meV [19–21]. Although the nature of this non-resonant coupling mechanism is not yet clear, we believe that it is connected to the charging of QDs in PC nanostructures due to surface trapping at the PC air holes.

2. Sample fabrication and experiment

The samples investigated are grown by molecular beam epitaxy and the layer structure is depicted schematically in figure 1(a). An undoped 500 nm thick $Al_{0.8}Ga_{0.2}As$ layer is deposited on a semi-insulating GaAs substrate, followed by a nominally 180 nm thick GaAs waveguide structure. A single layer of self-assembled $In_{0.5}Ga_{0.5}As$ QDs is incorporated at the centre of this waveguide. We stopped the rotation of the wafer during the QD growth to obtain a material gradient across the wafer and, therefore, regions with sufficiently low QD density suitable for single dot spectroscopy. The PC nanostructures were realized by a combination of electron beam lithography and reactive ion etching. Missing hole defect cavities consisting of three holes in a row, so-called L3 cavities [22], or reduced-symmetry single missing hole defect cavities, so-called Y1 cavities [23], have been established. Typical scanning electron microscope (SEM) and atomic force microscope (AFM) images of the PC are presented in figure 1(b). In a final processing step, the $Al_{0.8}Ga_{0.2}As$ sacrificial layer was removed by wet chemical etching (using hydrofluoric acid) to form free-standing membranes with symmetric semiconductor–air interfaces along the growth direction.

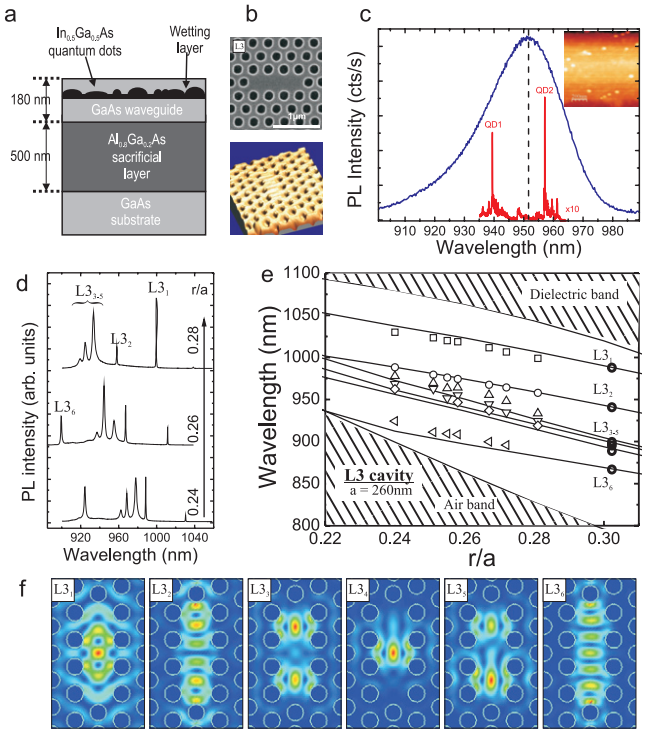

Figure 1. (a) Layer sequence of the QD sample. (b) SEM and AFM images of a typical PC nanostructure with an L3 line defect. (c) Comparison of QD ensemble (blue) and single QD (red) PL spectra. (d) Cavity mode emission of an L3 cavity for various r/a ratios. Corresponding 3D photonic band structure calculations (e) exhibit good agreement with the measurements. (f) Calculated D-field distribution of different L3 cavity modes.

The optical investigations were performed using a μ-PL setup with a spatial resolution of ∼700 nm. The sample was mounted in a helium-flow cryostat (at 15 K) and optically excited perpendicular to the sample surface by either pulsed (2 ps duration pulses, $f = 80$ MHz) or cw Ti:sapphire lasers. The luminescence was collected by a 100× microscope objective (numerical aperture = 0.8) and spectrally dispersed by either a 0.5 m imaging spectrometer (Jobin Yvon TRIAX 550) or a double monochromator (SPEX 1403). The signal was detected by either a liquid-nitrogen-cooled silicon charge coupled device (CCD) for μ-PL experiments or a fast silicon avalanche photodiode (SPAD) for time-resolved spectroscopy. A pair of similar SPADs in a Hanbury-Brown and Twiss configuration is used for determining the temporal statistics of the SE from single dots and the cross-correlation signal between different quantum emitters.

3. Results and discussion

In figure 1(c), we contrast typical μ-PL spectra from single QDs (red trace) and QD ensembles (blue trace). Ensembles with a high QD density exhibit an inhomogeneously broadened emission peak with a maximum intensity at $\lambda_{max} = 952$ nm, reflecting QDs with different sizes, shapes and material compositions. In strong contrast, single QDs give rise to sharp, spectrally well-separated emission lines ($\lambda_{QD1} = 939.3$ nm,

$\lambda_{QD2} = 957.1$ nm) corresponding to different transitions of their discrete energy levels [26]. The broadband emission of the QD ensemble sample is useful for the optical characterization of the PC nanocavity modes. The L3 nanocavities give rise to six distinct cavity modes (figure 1(d)), which can be controlled during the fabrication process via the so-called r/a ratio, where r and a denote the radius of the air holes and the lattice constant, respectively. In figure 1(d), we present three μ-PL spectra, where the radius r is increased from the bottom to the top trace from $r/a = 0.24$ to $r/a = 0.28$, respectively, for $a = 260$ nm. One can clearly distinguish that the six sharp and distinct peaks which correspond to the different cavity modes of the L3 cavity shift towards shorter wavelength for increasing r/a ratio, since the effective length of the cavity reduces with increasing air hole radius. For better control of the cavity emission, we performed three-dimensional calculations of the photonic band structure for such an L3 cavity. The results of these calculations are presented in figure 1(e), where we plot the wavelength as a function of the r/a ratio. The shaded region corresponds to the continuum band edges, which are termed the dielectric and air bands at long and short wavelengths, respectively. The white region between the continuum bands is the PBG and the different lines correspond to the different cavity modes. The cavity modes shift clearly to shorter wavelength for increasing r/a ratio and their wavelength is in very good agreement with the measurements shown in figure 1(d). The symbols in figure 1(e) represent measurements of all six cavity modes for varying r/a ratio and show good qualitative and quantitative accordance with the performed calculations. This allows us to simulate the emission of the PC nanocavities very accurately before the fabrication process, which therefore enables us to control the cavity modes with respect to the QD emission. The calculations of the D-field distribution presented in figure 1(f) indicate that the light field is strongly confined within the defect cavity region for all six cavity modes and, therefore, that these structures are very promising for realizing nanocavities with low mode volume and high quality (Q) factors. In our experiments Q factors of the order of 10^4 have been realized with this kind of cavity by engineering the in-plane confinement by shifting the outer holes away from their lattice sites, a technique first proposed by Akahane *et al* [22].

Using time-correlated single-photon counting we probe the SE dynamics of the embedded QD emission and, therefore, directly test the influence of the PC nanocavities and the PBG on the radiative dynamics of the QDs. An SEM image of the investigated PC cavity design is shown in figure 2(a). The cavity consists of a single missing hole defect with strongly reduced symmetry [23] and gives rise to ultra-low mode volumes $V = 0.5(\lambda/n)^3$ and Q factors $> 10^4$. The nanocavity, the body of the PC, the membrane and the bulk GaAs are indicated by white circles and denoted by the regions labelled (i)–(iv) in figure 2(a), respectively. A typical cw μ-PL spectrum from position (i) for low excitation powers ($P < 1$ μW) is shown in figure 2(b) (grey curve). Due to the Purcell effect, QDs spatially and spectrally coupled to the nanocavity emit preferentially into the cavity mode ($\lambda_{cav} = 1000 \pm 2$ nm), which exhibits a Q factor of $Q \sim 6500$. The emission of the

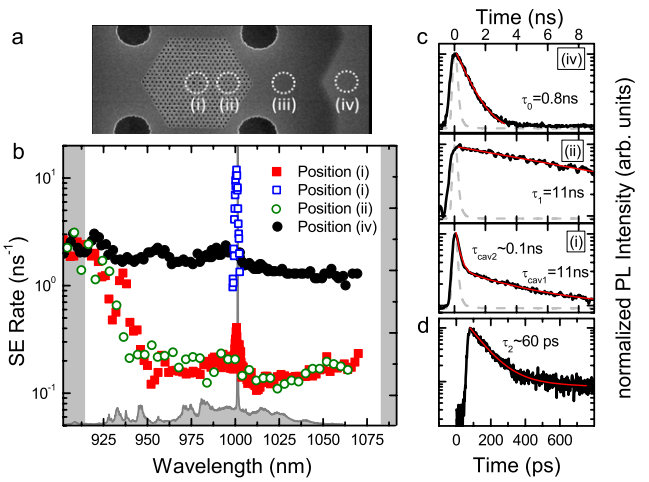

Figure 2. (a) Overview SEM image of a Y1 nanocavity indicating the cavity site (i), the body of the PC (ii), the free-standing membrane (iii) and the unprocessed bulk GaAs (iv) next to the PC. (b) SE rate as a function of the detection wavelength λ_{det} for positions (i)–(iv). (c) Corresponding time transients for positions (i)–(iv). (d) Ultra-fast time decay transient measured by a streak camera.

QD ensemble is observed as a weak background over the whole wavelength range. As a reference we determined the SE rate of QDs next to the PC region in the bulk, unpatterned GaAs (iv) and plotted the result in figure 2(b) (black circles). The SE rate stays almost constant at $\tau_0^{-1} \sim 1.31 \pm 0.02$ ns^{-1} over the whole spectral range from 902 to 1070 nm and the decay transients are clearly mono-exponential as shown in figure 2(c) (upper panel). Similar results are obtained from QDs in the unpatterned free-standing membrane (iii) (not shown here). In strong contrast, upon moving onto the body of the PC (ii) we observe a drastic change of the SE dynamics. The decay transients stay clearly mono-exponential (figure 2(c) (middle panel)), however, with a significantly reduced decay rate of $\tau_1^{-1} = 0.10 \pm 0.02$ ns^{-1}. The spectral dependence of this decay rate is shown in figure 2(b) (open green circles) and exhibits a pronounced transition from ~1 to 0.1 ns^{-1} as the detection wavelength λ_{det} is tuned from 910 to 940 nm. Calculations of the photonic bands (grey shaded regions in figure 2(b)) reveal that this pronounced change of the SE rate corresponds to moving from outside to inside the PBG and reflects the reduction of the local photonic density of states. Finally, we performed similar time-resolved measurements as a function of λ_{det} on the position of the defect nanocavity (i). The overall behaviour of the SE rate is very similar to the one obtained from the body of the PC. However, for detection wavelengths that are spectrally matching the nanocavity mode at λ_{cav} we observe a strong increase of the SE by a factor of 100×. This pronounced enhancement of the SE rate is due to the Purcell effect for QDs both spatially and spectrally in resonance with the nanocavity mode. In strong contrast to the case discussed above, in the spectral vicinity of the nanocavity mode we observe clear bi-exponential decays (cf figure 2(c) (bottom panel)) with a lower decay rate $\tau_{cav1}^{-1} = 0.1 \pm 0.02$ ns^{-1} similar to the decay rates observed on the body of the PC and a higher decay rate $\tau_{cav2}^{-1} = 3$–10 ns^{-1} close to the resolution limit of

our system. The high SE rate stems from QDs, which are both spatially and spectrally well coupled to the cavity mode and the low SE rate originates from QDs which are spectrally in resonance with the cavity mode, but spatially only weakly coupled to the electric field confined inside the nanocavity. For similar samples not presented here, we have even observed SE rates of the order of $\tau_2^{-1} \sim 20\,\mathrm{ns}^{-1}$ (Purcell factor $F_\mathrm{P} = 18 \pm 5$) in resonance with the cavity mode as shown by the decay transient in figure 1(d), recorded using a streak camera with better temporal resolution close to 10 ps.

Besides the strong modification of the SE rate of the QD emission a PC nanostructure (even without a nanocavity) leads to a spatial redistribution of the emission [8]. Due to the PBG and the strongly reduced number of optical states, photons are preferentially emitted vertical to the plane of the PC, leading, therefore, to an enhanced optical extraction efficiency η. In figure 3(a) we compare the spatial dependence of the SE rate (lower panel) at different positions across the nanostructure, ranging from the nearby bulk GaAs (iv) to the nanocavity (i) spectrally detuned from the cavity mode, with the time-integrated emission intensity $\langle I \rangle_t$ under pulsed excitation (upper panel). When moving the detection spot from the bulk GaAs (iv) onto the underetched membrane (iii) the SE rate stays constant at τ_0^{-1} $1.25 \pm 0.05\ \mathrm{ns}^{-1}$, whereas $\langle I \rangle_t$ drops by a factor of $\sim 3.8\times$ due to efficient waveguiding in the membrane. As soon as we move onto the body of the PC, the SE rate decreases by approximately a factor of $10\times$, whereas simultaneously $\langle I \rangle_t$ increases by a similar factor with respect to dots in the unpatterned bulk GaAs. Since $\langle I \rangle_t$ is a direct measure of the photon extraction efficiency, this result clearly demonstrates the effect of efficient spatial redistribution of photons due to the PBG. We conclude that photons from QDs emitting inside the PBG are collected much more efficiently than from QDs in the unpatterned region of the sample, which could drastically improve applications where the external quantum efficiency is crucial, such as efficient light emitters [24] and single-photon sources [25, 10].

We checked these conclusions by performing pulsed PL measurements on single QDs emitting inside and outside the PBG, respectively. Figure 3(b) (right panel) compares low power PL spectra recorded from two dots, one within the unpatterned membrane (QD1, $\lambda_{\mathrm{QD1}} = 921.4$ nm) and a second (QD2, $\lambda_{\mathrm{QD2}} = 954.2$ nm) within the cavity, but spectrally detuned from the cavity mode. Power-dependent measurements allow us to identify the single exciton transitions for both dots from the linear behaviour of their intensities as a function of excitation power (figure 3(b)—left panel). Power-dependent measurements performed with a repetition frequency of 80 MHz show saturation of the average PL intensity above $P_\mathrm{sat} = 2 \times 10^3$ nW for both dots. The intensity of QD1 saturates at $I_\mathrm{satPC} = 3 \times 10^4$ cps, whereas the bulk QD emission saturates already at $I_\mathrm{satbulk} = 6 \times 10^3$ cps. The ratio $I_\mathrm{satPC}/I_\mathrm{satbulk} \sim 5$ is a direct measure for the enhancement of the extraction efficiency and is in excellent agreement with the ensemble QD studies presented above. This measurement confirms that the 2D-PC alone strongly enhances the single-photon extraction efficiency from self-assembled QDs [10].

As already mentioned in the introduction, efficient single-photon sources are essential for many applications in quantum

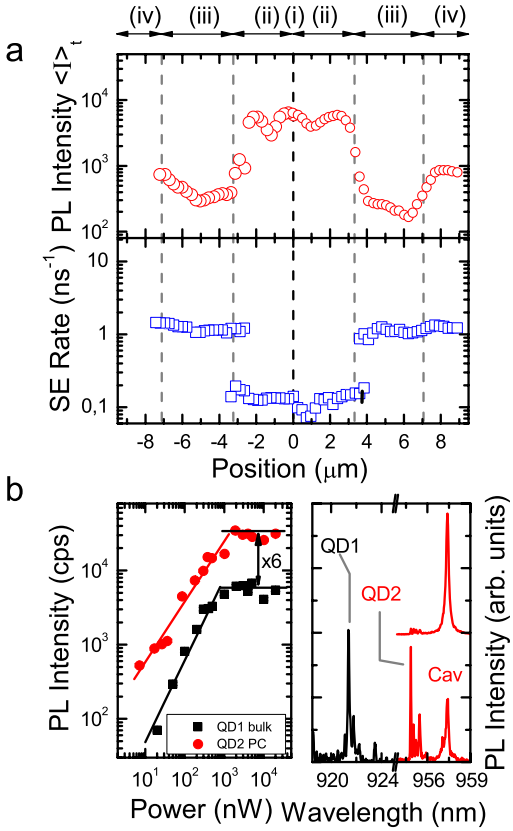

Figure 3. (a) SE rates as a function of the detection position (lower panel) and corresponding time-integrated PL intensity (upper panel). (b) (Left panel) Power-dependent μ-PL measurement of single QDs next to the PC (black squares) and in the body of the PC (red circles) showing $6\times$ enhanced extraction efficiency. (Right panel) Corresponding PL spectra for low (bottom) and high (top) excitation powers.

information processing. Although QDs coupled to PC nanocavity modes offer a great opportunity for realizing such devices, it is technologically challenging to obtain strong *spatial* and *spectral* coupling of the QD emission to the cavity mode. An alternative is to use QDs in PC and exploit the spatial redistribution of the emission to enhance the single-photon extraction efficiency. We showed already in figure 3(b) that this concept indeed works for single QDs by performing power-dependent photoluminescence measurements. In figure 4(a) we present PL spectra of a single QD spectrally detuned from the cavity mode as a function of excitation power density P_ext. At $P_\mathrm{ext} = 8\ \mathrm{W\,cm}^{-2}$, we observe several sharp emission lines, all stemming from different transitions of the same QDs. The emission line at $\lambda = 940.3$ nm (red line) shows a clear linear power dependence with a slope $m_{1\mathrm{X}^*} = 0.96$, which indicates that this state corresponds to a single exciton transition of the QD. Measuring the temporal statistics of the QD emission using a conventional Hanbury-Brown–Twiss type photon correlation setup results in strong photon antibunching as shown in the lowest trace in figure 4(b). The peak at zero time delay between both single-photon counting modules is strongly reduced compared to the adjacent peaks. The area of the peak at $\tau_1 - \tau_2 = 0$ is a direct measure of the multiphoton emission probability, a figure of merit that

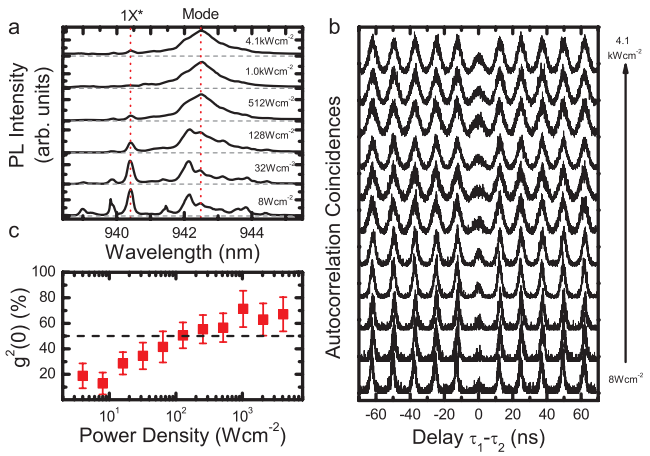

Figure 4. (a) μ-PL intensity of a single QD ($1X^*$) detuned from the cavity mode as a function of applied excitation power density. (b) Corresponding photon correlation measurements of 1X* as a function of power density. (c) Summary of the photon antibunching $g^{(2)}(0)$ as a function of the power density.

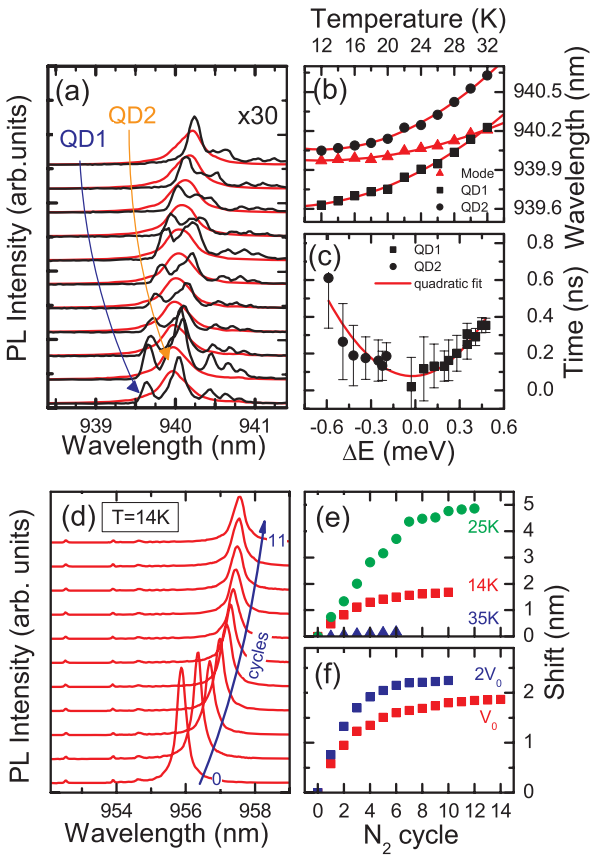

Figure 5. (a) Temperature-dependent μ-PL measurements for a single QD–cavity system for low (black) and high (red) excitation power. (b) Extracted wavelength positions of cavity mode (red triangles), QD1 (squares) and QD2 (circles). (c) Time-resolved measurements on QD1 (squares) and QD2 (circles) as a function of QD–cavity detuning. (d) μ-PL spectra of a cavity mode as a function of introduced nitrogen. (e) Cavity mode wavelength shift for various temperatures T: 14 K (red squares), 25 K (green circles) and 35 K (blue triangles). (f) Cavity mode wavelength shift for two different volumes V_0 (red) and $2V_0$ (blue).

is commonly used to evaluate the purity of single-photon sources [6]. With a value of $g^{(2)}(0) = 18\%$ our single-photon source shows a clear signature of non-classical light emission. Furthermore, we plot in figure 4(b) the evolution of the photon antibunching as a function of the excitation power density from 8 W cm^{-2} up to 4.1 kW cm^{-2}. We observe that even for excitation power densities far above the saturation of the 1X* transition ($P_{\text{sat}} = 400$ W cm^{-2}) clear photon antibunching is observed. This finding is illustrated in figure 4(c) where we plot the normalized area of the $g^{(2)}(0)$ peak as a function of the excitation power density. For excitation power densities below 300 W cm^{-2} $g^{(2)}(0)$ is less than 50% which indicates that the light stems from one single quantum emitter. For higher excitation power densities the nearby cavity mode at $\lambda_{\text{cav}} = 942.5$ nm dominates the μ-PL spectrum. This leads to an enhancement of the background emission at the QD wavelength, as indicated by the grey dashed lines in figure 4(a). This background emission enhances the $g^{(2)}(0)$ value for higher excitation power densities and results in an increase of the multiphoton emission probability. Furthermore, we note that the peaks in the correlation spectrum broaden with increasing excitation power densities, an observation which is likely due to state filling effects in the population of the QD levels.

For more demanding applications such as linear optical quantum computation [2] it is preferable to use QDs which are coupled to a cavity mode and, therefore, exhibit strong Purcell enhancement since photons are emitted at a high rate and, thus, have a strong degree of quantum indistinguishability. Badolato and coworkers [27] demonstrated that it is, in principle, possible to deterministically position a single QD with respect to the electric field maximum of a PC nanocavity mode. However, this technique requires quite sophisticated nanofabrication with positioning precision better than 30 nm. Alternatively, one can use a moderate QD density in combination with a cavity-resonant excitation technique which predominantly excites QDs located at the electric field maximum inside the PC nanocavity [28]. In order to observe pronounced cQED effects it is equally important to tune the QD emission *spectrally* in resonance with the cavity mode. For such a purpose one can either tune the cavity frequency with respect to the dot frequency or vice versa.

Up to now the QD frequency has been mainly tuned by varying the lattice temperature of the semiconductor crystal (cf [15]). There, the QD frequency shifts to longer wavelength compared to the cavity mode. Such a scenario is depicted in figure 5(a), where we present μ-PL measurements of a single QD–cavity system for varying temperatures from $T = 12$ K (bottom) to $T = 32$ K (top). In red we plot high excitation power spectra, clearly indicating the cavity mode ($\lambda_{\text{cav}} = 939.95$ nm at 10 K). For a strongly reduced excitation power (black traces), we observe several different peaks, which all arise from the same quantum emitter. By increasing the temperature one can clearly see that the emission of the dot transitions labelled QD1 ($\lambda_{\text{QD1}} = 939.64$ nm at 10 K) and QD2 ($\lambda_{\text{QD1}} = 940.05$ nm at 10 K) shift with a higher rate towards longer wavelength compared to the cavity

emission. In figure 5(b) we plot the extracted peak positions of the cavity mode (red triangles), QD1 (black squares) and QD2 (black circles) as a function of the temperature, clearly demonstrating the behaviour discussed above. We performed time-resolved measurements on QD1 and QD2 (figure 5(c)) to trace the influence of the cavity mode on the spontaneous emission dynamics of the two dots investigated. Combining both datasets of QD1 and QD2, we obtain a curve which can be fitted by a quadratic function (red trace) which is a reasonable approximation of the expected Lorentzian fit for small detunings[1]. From this fit we extract a width of the cavity mode $\Delta E_{\mathrm{cav},\tau} = 0.50$ meV, which is in excellent agreement with the full width at half maximum of the cavity mode obtained from the μ-PL measurement of $\Delta E_{\mathrm{cav,PL}} = 0.55 \pm 0.05$ meV. This shows unambiguously the Purcell enhancement of the QD SE via the cavity mode. Although such a temperature tuning technique has been extensively used by many groups worldwide, it exhibits several disadvantages. First of all, the tuning range which can be obtained by this technique is limited to less than 2 nm, whereas one has to keep in mind that simultaneously the cavity mode itself shifts slowly to longer wavelength. However, the most severe problem is that, by increasing the temperature, one changes the dephasing and decoherence properties of the QD emission.

In addition, the *cavity* mode emission can be coarsely tuned during the fabrication process by varying the r/a ratio [29] of the PC or by a post-fabrication technique known as digital etching [17]. Both techniques provide tuning ranges of several tens of nanometres that are, however, accompanied by a lack of reversibility. A more convenient *in situ* technique for controlling the cavity mode wavelength was first demonstrated by Mosor *et al* in 2005 [18]. Here, one controllably introduces a small amount of inert gas (nitrogen, xenon) into the otherwise evacuated sample chamber of the cryostat through a capillary tube close to the sample surface. Subsequently, the gas freezes onto the cold surface of the PC and forms a thin layer of molecular nitrogen. This procedure effectively increases the length of the cavity and results in a small redshift of the cavity mode. As shown in the μ-PL spectra in figure 5(d), one can deterministically tune the cavity mode ($\lambda_{\mathrm{cav}} = 955.86$ nm) in precise steps towards longer wavelength whilst the QD emission (weak features below 955 nm) remains unaffected. One clearly observes a saturation of the shift and a simultaneous broadening of the cavity mode emission. The maximum shift Δ_{max} is strongly dependent on the temperature at which the gas is introduced into the cryostat, as depicted in figure 5(e). For nitrogen gas we observed an enhanced maximum shift when holding the sample at $T = 25$ K ($\Delta_{\mathrm{max,25\ K}} = 4.8$ nm, green circles), as compared to $T = 14$ K ($\Delta_{\mathrm{max,14\ K}} = 1.7$ nm, red squares). A further increase in temperature up to $T = 35$ K (blue triangles) results in no observable shift, most likely due to the desorption of the nitrogen from the membrane at elevated temperatures. The shift rate could be controlled by the amount of nitrogen introduced into the cryostat, as shown in figure 5(f) for two different injected volumes $V_0 = 2.1$ cm^3 and $2V_0 = 4.2$ cm^3. This thin film deposition technique allows for a deterministic and reversible control of the cavity mode over large wavelength ranges without strongly perturbing the emission properties of the QDs.

[1] We used a quadratic fit as an approximation of a Lorentzian for fitting the temperature-dependent time-resolved data, since we could not reach a saturation of the decay times due to the limited spectral tuning range.

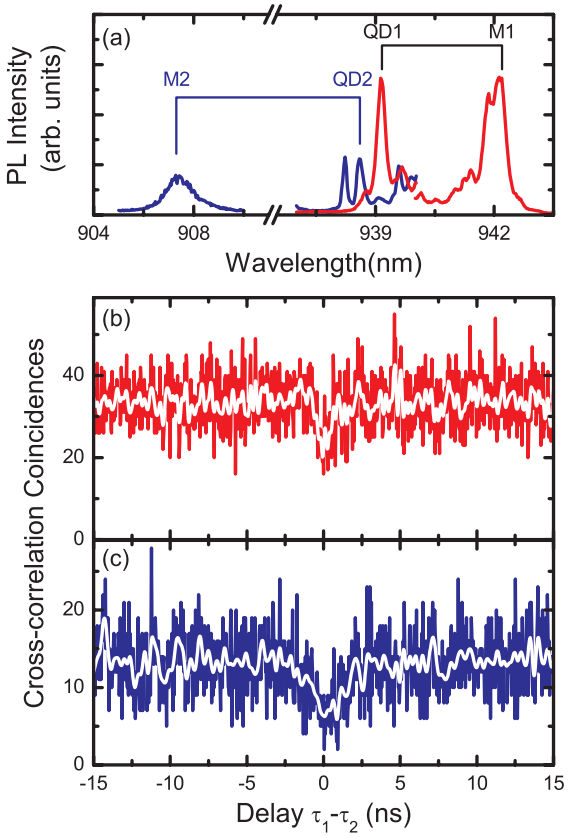

Figure 6. μ-PL spectra of QD–cavity system exhibiting non-resonant coupling between QD1/M1 and QD2/M2. Corresponding cross-correlation histograms for QD1/M1 and QD2/M2 are shown in (b) and (c), respectively. The white line is a five-point average fit of the measured data.

This technique enables us to probe the coupling between QDs and cavity mode in a controlled way. Most surprisingly, the emission from single QDs coupled to the cavity mode is found to be strongly altered when compared to QDs in bulk GaAs. For dots that are in resonance with the cavity mode, the photon antibunching obtained from autocorrelation measurements is strongly degraded as compared to the detuned case [21] due to an enhanced background emission from the cavity mode. Furthermore, for QDs detuned from the cavity mode we observe an unexpected non-resonant coupling mechanism between QD and mode [20, 19, 21]. A typical situation is depicted in figure 6(a), which shows the PL spectra of two cavity modes (M1 and M2) and different QD states (QD1 and QD2). Cross-correlation measurements performed between QD1 and M1 as well as between QD2 and M2 have been performed and corresponding correlation histograms are shown in figures 6(b) and (c), respectively. Both measurements show a dip in the cross-correlation spectrum at $\tau_1 - \tau_2 = 0$, indicating correlations for the respective QD–cavity system. These measurements show evidence for

an unknown and, up to now, not fully understood remote coupling mechanism between QD emission and PC cavity mode which has been shown to be active for energy detunings $\Delta E = E_{\mathrm{cav}} - E_{\mathrm{QD}} > 10$ meV. Similar findings have been reported by Hennessy *et al* for PC [19] and Press *et al* for micropillar cavities [20] in the strong coupling regime. The underlying mechanism of this coupling process is still under investigation, whilst one possible mechanism based on highly charged QDs due to charge trapping at etched surfaces suggests photon-mediated shake-up-like processes (similar to [30]) and is discussed in more detail in [21]. The non-resonant coupling between a QD and a cavity mode may constitute a major hindrance in realizing an efficient single-photon source based on QDs coupled to PC nanocavities. Thus, the development of a complete understanding of this mechanism is necessary to realize such devices. This remote coupling mechanism may also play a significant role in the operation of high-β nanolasers, as it may control the gain characteristics [31].

4. Conclusions and outlook

In summary, in this review we presented studies of single QD–cavity systems based on self-assembled $In_{0.5}Ga_{0.5}As$ QDs embedded in 2D PCs and defect nanocavities. We showed that photonic nanostructures represent a strongly modified photonic environment for the QD SE and by coupling dots to low mode volume, high Q nanocavities they can exhibit pronounced Purcell enhancements ($F_{\mathrm{P}} = 18 \pm 5$). QD ensemble and single QD measurements show the potential to realize efficient devices, for example single-photon sources, based on a spatial redistribution of the QD emission due to the PBG. A 6–10× enhancement of the photon extraction efficiency has been demonstrated along with pronounced single-photon emission of single dots emitting into the PBG ($g^{(2)}(0) = 18\%$). The need for spectral tuning is inherent for coupled single-dot–cavity systems and has been discussed on the basis of spectrally tuning the *emitter* via temperature and/or the *cavity mode* by applying a gas deposition technique. On the way to an efficient single-photon source based on a single QD spectrally and spatially coupled to a PC nanocavity mode, one has to overcome a phenomenon which leads to non-resonant coupling between emitter and mode even for large spectral detunings (>19 meV). This leads to a drastic enhancement of the multiphoton emission probability due to background emission and, therefore, destroys the purity of the single-photon source. The understanding of this mechanism, which conflicts with the so-far successfully applied *artificial atom* picture of QDs, is fundamental for realizing such non-classical devices.

For the future, we believe that the implementation of such PC nanocavities into electrically tunable devices [16] is most crucial. This provides a deterministic and fast way to control the emission energy of the QD over an energy range of a few meV. Recently, the electrical manipulation of single QDs coupled to PC nanocavities in the weak and strong coupling regime has been successively demonstrated [32]. Furthermore, the implementation of lateral electric fields in those structures promises another route to control the dot–cavity detuning and the efficient emission of entangled photon pairs [33] by tuning the exciton and bi-exciton energy into resonance [34]. These lateral electric fields could be applied to coupled PC resonator structures that enable the specific control of different quantum emitters in nearby resonators coupled via an optical field [35].

Acknowledgments

We acknowledge financial support of the Deutsche Forschungsgemeinschaft via the Sonderforschungsbereich 631, Teilprojekt B3 and the German Excellence Initiative via the 'Nanosystems Initiative Munich (NIM)'.

References

[1] Gisin N, Ribordy G, Tittel W and Zbinden H 2002 *Rev. Mod. Phys.* **74** 145
[2] Knill E, Laflamme R and Milburn G J 2001 *Nature* **409** 46
[3] Dür W, Briegel H-J, Cirac J I and Zoller P 1999 *Phys. Rev.* A **59** 169
[4] Michler P, Kiraz A, Becher C, Schoenfeld W V, Petroff P M, Zhang L, Hu E and Imamoğlu A 2000 *Science* **290** 2282
[5] Santori C, Pelton M, Solomon G, Dale Y and Yamamoto Y 2001 *Phys. Rev. Lett.* **86** 1502
[6] Zwiller V, Aichele T and Benson O 2004 *New J. Phys.* **6** 96
[7] Yablonovitch E 1987 *Phys. Rev. Lett.* **58** 2059
[8] Fujita M, Takahashi S, Tanaka Y, Asano T and Noda S 2005 *Science* **308** 1296
[9] Kaniber M, Kress A, Laucht A, Bichler M, Meyer R, Amann M-C and Finley J J 2007 *Appl. Phys. Lett.* **91** 061106
[10] Kaniber M, Laucht A, Hürlimann T, Bichler M, Meyer R, Amann M-C and Finley J J 2008 *Phys. Rev.* B **77** 073312
[11] Kress A, Hofbauer F, Reinelt N, Kaniber M, Krenner H J, Meyer R, Böhm G and Finley J J 2005 *Phys. Rev.* B **71** 241304(R)
[12] Purcell E M 1946 *Phys. Rev.* **69** 681
[13] Santori C, Fattal D, Vučkovic J, Solomon G S and Yamamoto Y 2002 *Nature* **419** 594
[14] Laurent S, Varoutsis S, Le Gratiet L, Lemaître A, Sagnes I, Raineri F, Levenson A, Robert-Philip I and Abram I 2005 *Appl. Phys. Lett.* **87** 163107
[15] Kiraz A, Michler P, Becher C, Gayral G, Imamoğlu A, Zhang L, Hu E, Schoenfeld W V and Petroff P M 2001 *Appl. Phys. Lett.* **78** 3932
[16] Hofbauer F, Grimminger S, Angele J, Böhm G, Meyer R, Amann M-C and Finley J J 2007 *Appl. Phys. Lett.* **91** 201111
[17] Hennessy K, Badolato A, Tamboli A, Petroff P M, Hu E, Atatüre M, Dreiser J and Imamoğlu A 2005 *Appl. Phys. Lett.* **87** 021108
[18] Mosor S, Hendrickson J, Richards B C, Sweet J, Khitrova G, Gibss H M, Yoshie T, Scherer A, Shchekin O B and Deppe D G 2005 *Appl. Phys. Lett.* **87** 141105
[19] Hennessy K, Badolato A, Winger M, Gerace D, Atatüre M, Gulde S, Fält S, Hu E L and Imamoğlu A 2007 *Nature* **445** 896
[20] Press D, Götzinger S, Reitzenstein S, Hofmann C, Löffler A, Kamp M, Forchel A and Yamamoto Y 2007 *Phys. Rev. Lett.* **98** 117402
[21] Kaniber M, Laucht A, Neumann A, Villas-Bôas J M, Bichler M, Amann M-C and Finley J J 2008 *Phys. Rev.* B **77** 161303(R)
[22] Akahane Y, Asano T, Song B-S and Noda S 2003 *Nature* **425** 944
[23] Vučkovic J and Yamamoto Y 2003 *Appl. Phys. Lett.* **82** 2374
[24] Bennett A J, Unitt D C, See P, Shields A J, Atkinson P, Cooper K and Ritchie D A 2005 *Appl. Phys. Lett.* **86** 181102

[25] Pelton M, Santori C, Vučkovic J, Zhang B, Solomon G S, Plant J and Yamamoto Y 2002 *Phys. Rev. Lett.* **89** 233602
[26] Finley J J, Ashmore A D, Lemaître A, Mowbray D J, Skolnick M S, Itskevich I E, Maksym P A, Hopkinson M and Krauss T F 2001 *Phys. Rev.* B **63** 073307
[27] Badolato A, Hennesssy K, Atatüre M, Dreiser J, Hu E, Petroff P M and Imamoğlu A 2005 *Science* **308** 1158
[28] Kaniber M, Neumann A, Laucht A, Bichler M, Amann M-C and Finley J J 2008 *Preprint* 0803.2403v1 [cond-mat.mes-hall] under consideration
[29] Kress A, Hofbauer F, Reinelt N, Kaniber M, Bichler M, Schuh D, Böhm G and Finley J J 2005 *Proc. SPIE Int. Soc. Opt. Eng.* **5733** 114–24
[30] Karrai K, Warburton R J, Schulhauser C, Hoğele A, Urbaszek B, McGhee E J, Govorov A O, Garcia J M, Gerardot B D and Petroff P M 2004 *Nature* **427** 135
[31] Strauf S, Hennessy K, Rakher M T, Choi Y-C, Badolato A, Andreani L C, Hu E L, Petroff P M and Bouwmeester D 2006 *Phys. Rev. Lett.* **96** 127404
[32] Hofbauer F, Laucht A, Stobbe S, Angele J, Kaniber M, Böhm G, Lodahl P, Amann M-C and Finley J J 2008 *Nature* in preparation
[33] Stevenson R M, Young R J, Atkinson P, Cooper K, Ritchie D A and Shields A J 2006 *Nature* **439** 179
[34] Clark E C 2008 *Appl. Phys. Lett.* in preparation
[35] Englund D, Faraon A, Zhang B, Yamamoto Y and Vučkovic J 2007 *Opt. Express* **15** 5550